Yan, Dongni; Mikkola, Tommi; Kujala, Pentti; Hirdaris, Spyros

Hydroelastic analysis of slamming induced impact on stiff and flexible structures by two-way CFD-FEA coupling

Published in:
Ships and Offshore Structures

DOI:
10.1080/17445302.2022.2116231

Published: 17/08/2023

Ships and Offshore Structures

ISSN: (Print) (Online) Journal homepage: https://www.tandfonline.com/loi/tsos20

Hydroelastic analysis of slamming induced impact on stiff and flexible structures by two-way CFD-FEA coupling

Dongni Yan, Tommi Mikkola, Pentti Kujala & Spyros Hirdaris

To cite this article: Dongni Yan, Tommi Mikkola, Pentti Kujala & Spyros Hirdaris (2023) Hydroelastic analysis of slamming induced impact on stiff and flexible structures by two-way CFD-FEA coupling, Ships and Offshore Structures, 18:9, 1300-1312, DOI: 10.1080/17445302.2022.2116231

To link to this article: https://doi.org/10.1080/17445302.2022.2116231

SHIPS AND OFFSHORE STRUCTURES
2023, VOL. 18, NO. 9, 1300–1312
https://doi.org/10.1080/17445302.2022.2116231

Hydroelastic analysis of slamming induced impact on stiff and flexible structures by two-way CFD-FEA coupling

Dongni Yan, Tommi Mikkola, Pentti Kujala and Spyros Hirdaris

Marine Technology Group, Department of Mechanical Engineering, Aalto University, Espoo, Finland

ABSTRACT

In rough seas, ships may be subject to wave-induced slamming loads. Thus, modelling of fluid and structural mechanics, and their dynamic interactions can help with the evaluation of fluid actions and the prediction of wave-induced loads for use in ship design. In this paper a partitioned two-way coupled CFD-FEA fluid–structure interaction (FSI) method is used to study the water entry of flat plates with different impact velocities and wedges with different deadrise angles. Results show that when flexible plate dynamics prevail, at relatively low to medium impact velocity a negative correlation between the nondimensional pressure and water entry velocities is evident near plate centre areas. A steady correlation exists when only stiff plate dynamics prevail. Pressure differences between stiff and flexible wedges become evident at small deadrise angles. The similarity of the pressure distribution during water impingement of ideally stiff wedge structures is not valid when structural flexibility prevails.

ARTICLE HISTORY
Received 5 November 2021
Accepted 17 August 2022

KEYWORDS
Slamming loads; hydroelasticity; fluid–structure interactions (FSI); two-way coupling; ship design

1. Introduction

When a ship operates in rough seas, her bow may lift and then slap on waves because of the relative motions between the hull and the wave surface. Due to high vertical velocity during the re-entry of the ship hull in water, impulsive loads associated with the high hydrodynamic pressure peaks occur. This phenomenon is called 'slamming' and it is strongly nonlinear. Local slamming loads are severe, transient and may cause local structural damage during extreme events (Hirdaris et al. 2014). For example, Yamamato et al. (1985) reported damages due to bow flare slamming on an 819 TEU container ship in cyclone conditions. They concluded that an 840 kPa impact pressure in way of a 13.7 m circular area, may lead to structural damage. The adverse effects of an extreme slamming case influenced the M/S Estonia accident in 1994. During her last journey in Baltic Sea, due to slamming the ship lost her bow visor (JAIC 1997). A damage of her watertight front door led to her capsize and the loss of 852 lives.

A comprehensive research summary on ship slamming is presented by Kapsenberg (2011). Early research on local slamming loads has been driven by von Karman (1929) and Wagner (1932). Wagner's model is based on the potential flow theory. It applies within the context of ideal and incompressible fluid flow that is generally used for the estimation of the pressure distribution on two-dimensional ideally stiff bodies (e.g. ideally stiff wedges).

Zhao and Faltinsen (1993) solved the similarity flow for wedges by a nonlinear boundary element method with a jet flow approximation. Their results agreed with the simple asymptotic solution by Wagner (1932) for small deadrise angles. Zhao et al. (1996) extended this approach to 2D arbitrary geometries. These papers provided important research output in terms of the value of analytical formulations and potential flow-based simulations and the ideas presented are implemented in existing classification guidelines (DNVGL 2017).

With the advent of super-computing power, advanced numerical methods have been employed to better understand the influence of fluid-induced nonlinearities. Examples are the Arbitrary Lagrangian-Eulerian (ALE) scheme (Stenius et al. 2006; Wang and Guedes Soares 2012), the Finite Volume Method (FVM) (Southall et al. 2015), Smoothed Particle Hydrodynamics (SPH) (Alexandru et al. 2007; Veen and Gourlay 2012; Farsi and Ghadimi 2016) and Volume of Fluid (VOF) methods (Southall et al. 2014). Maki et al. (2011) presented a loosely coupled CFD-FEA method to study the water entry of an elastic wedge. In their work, CFD is applied to obtain the slamming pressures on an ideally stiff body. Consequently, the pressure is projected onto a structural FEM model. Hydroelastic coupling approaches have been carried out to study the influence of flexible fluid–structure interactions on wedge-shape structures by combining the Boundary Element Methods (BEM) and Finite Element Method (FEM) (e.g. Lu et al. 2000), ALE and FEM (Stenius et al. 2011; Wang and Guedes Soares 2014) and SPH and FEM (Panciroli et al. 2012). Recently, Truong et al. (2021) conducted a benchmark study on the analysis of slamming responses of flat-stiffened plates. The authors compared successfully different numerical methods that may be used for the analysis of local slamming loads. Yan et al. (2022) presented a detailed validation of two-way coupled Finite Volume (FVM) and FEA methods. The authors studied the full history of the flat plate water entry problem. Experimental and numerical uncertainties analysed according to ASME V&V method (ASME 2009) confirmed the validity of the simulation-based approach.

In literature, there is lack of systematic comparisons on how different the behaviours of stiff and flexible structures can be by considering the strong-coupled FSI. With the latter in mind, this paper extends the work by Yan et al. (2022) for the case of stiff and flexible plates impinging the water at different impact velocities and wedges impinging the water at different deadrise angles. The mechanics of the two-way coupled FVM-based CFD and FEA methods are systematically analysed to further study the influence of structural dynamics on the loads and responses. The effects of

CONTACT Spyros Hirdaris spyros.hirdaris@aalto.fi Marine Technology Group, Department of Mechanical Engineering, Aalto University, Espoo 02150, Finland
This article has been corrected with minor changes. These changes do not impact the academic content of the article.

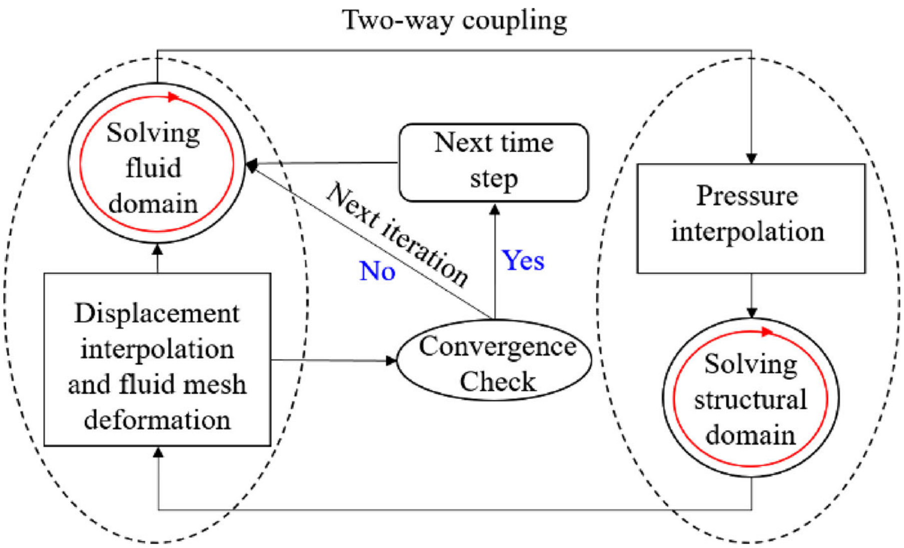

Figure 1. Two-way coupled FSI modelling method. (This figure is available in colour online).

slamming are analysed within the context of two-phase flow idealisation (i.e. air and water effects are considered). For the wedge structure, results are compared against classification guidelines (DNVGL 2017).

The rest of the paper is organised as follows. Section 2 describes the hydroelastic modelling methodology. Section 3 presents numerical investigations and discussion. Conclusions are drawn in Section 4.

2. Hydroelastic modelling

In slamming problems, both impact and responses are transient and strongly interactive. This is because the variation of fluid actions may modify the dynamic state of the structure, and consequently nonlinear motions may lead to stochastic responses. Hydroelastic models may be considered useful in terms of studying on the dynamic response (Hirdaris and Temarel 2009). Two-way coupled flexible fluid–structure interaction models may lead to more realistic results (e.g. Kivelä et al. 2020; Lakshmynarayanana and Hirdaris 2020).

The simulations presented in this paper are based on the two-way coupled partitioned approach of Lakshmynarayanana and Hirdaris (2020) (see Figure 1). The fluid domain is idealised by FVM and accordingly the flow is assumed to be governed by (i) the continuity equation described by mass conservation and (ii) Navier-Stokes equations following the principles momentum conservation (Ferziger and Peric 2003) as embedded in STAR CCM+ 13.02 (2018). Structural idealisations are carried out in FEA solver ABAQUS (Dassault Systèmes 2016). Throughout the simulations, both fluid pressure and structural displacement were constantly transferred in between the FSI boundaries, while fluid mesh deformations were accounted for at each time step. A detailed discussion on fluid and structural domain modelling and their interactions is given in the following sub-sections.

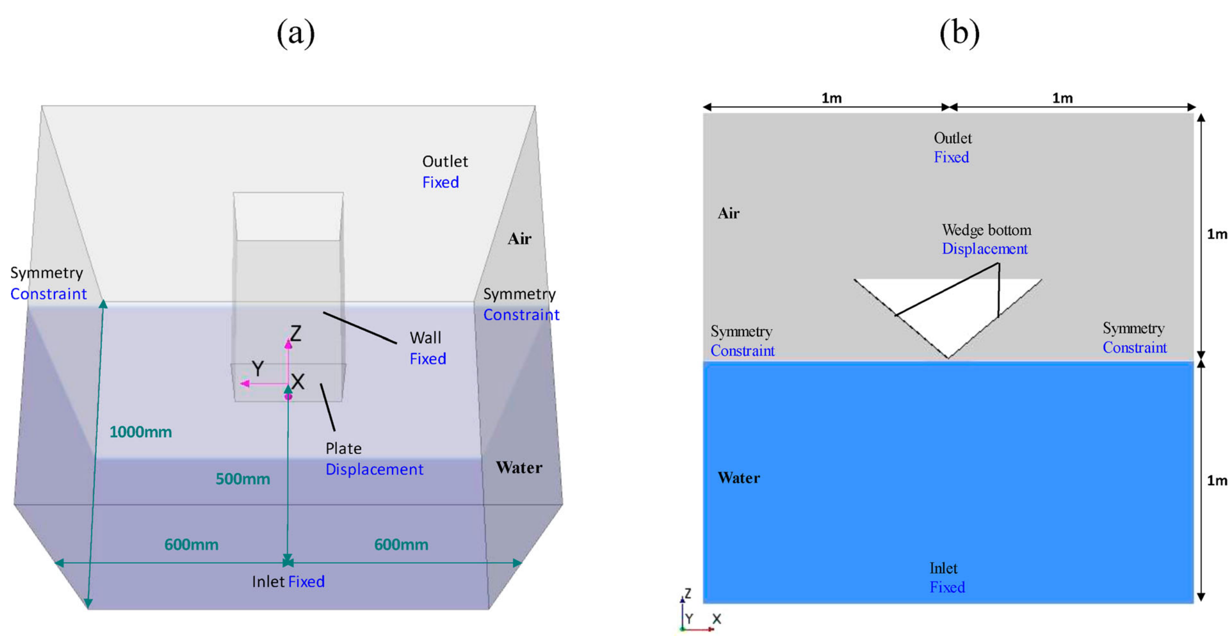

Figure 2. Fluid domain idealisation (a) plate and (b) wedge. (This figure is available in colour online).

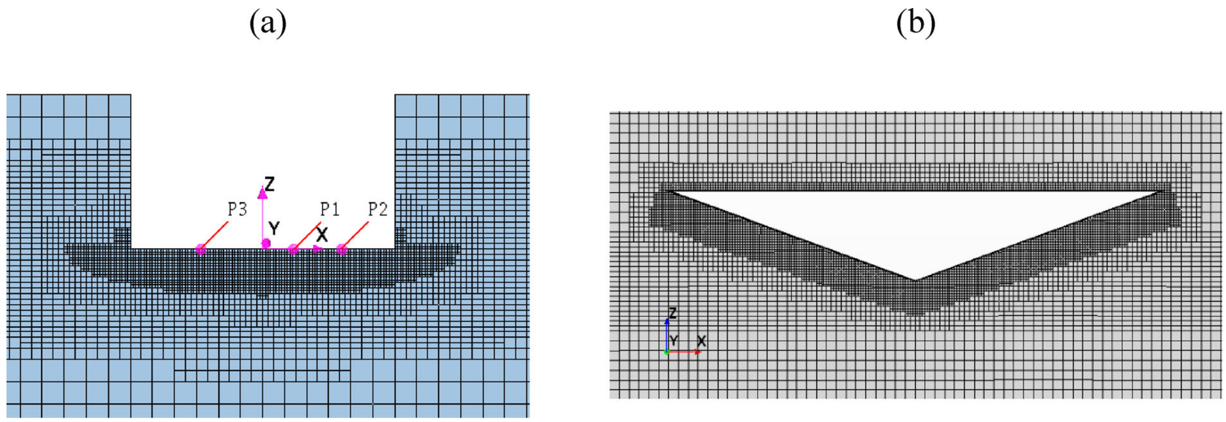

Figure 3. Mesh discretisation around (a) plate and (b) wedge. (This figure is available in colour online).

Table 1. Material properties.

	Stiff plate	Stiff wedge	Flexible plate	Flexible wedge
Material	Aluminium		Polyoxymethylene (POM)	
Young's modulus (MPa)	70,300		2800	
Poisson's ratio	0.33		0.3	
Shear modulus (MPa)	26,400		1077	
Density (kg/m^3)	2660		1410	
Thickness (mm)	16	16	4.7	6.3

2.1. Fluid domain modelling

The fluid domain idealisations of plate and wedge models are depicted in Figure 2. For the case of the plate structure, the reference domain is based on Tödter et al. (2020). To develop an accurate and computationally efficient FSI domain for the prediction of slamming forces, instead of modelling the exact test tank sizes, the 3D computational domain was idealised as a cuboid of length 1200 mm in both x- and y-directions, and with height of 1000 mm in the z-direction (see Figure 2(a)). The position of the

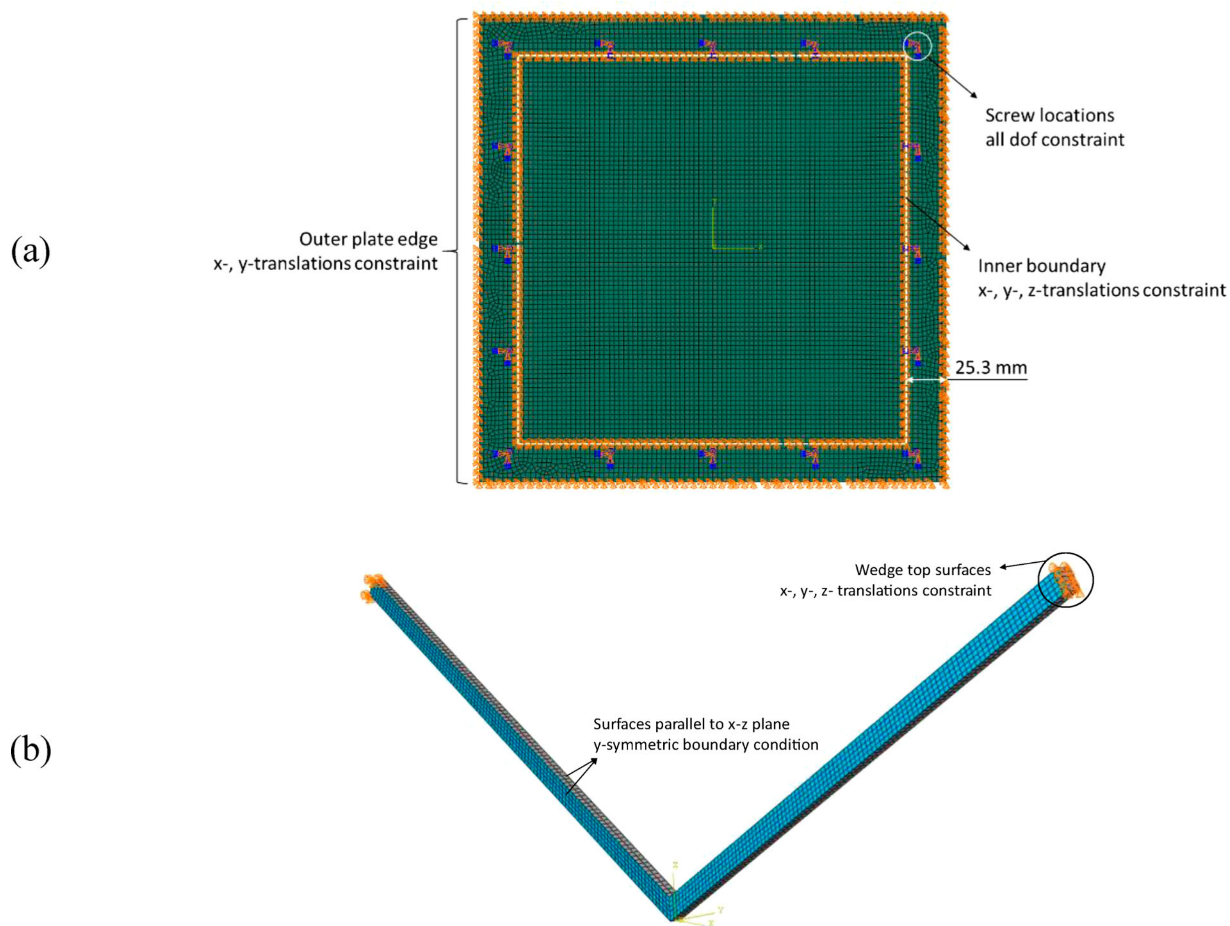

Figure 4. FEA models with eight-node continuum shell elements (ABAQUS SC8R) and structural boundary conditions for (a) plate and (b) wedge. (This figure is available in colour online).

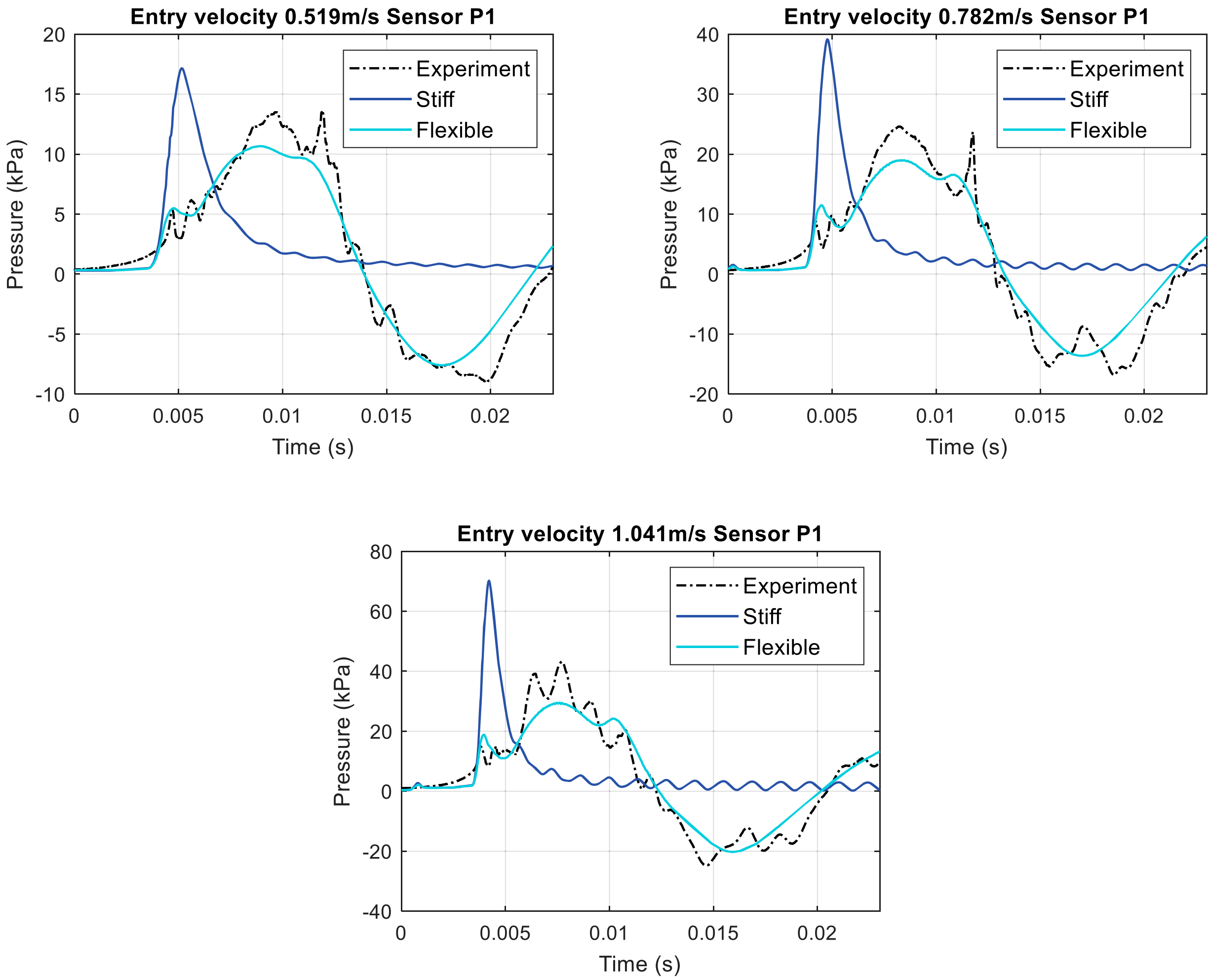

Figure 5. Comparison of stiff and flexible plate simulations with experimental (flexible plate) results presented by Tödter et al. (2020) for different entry velocities namely 0.519, 0.782 and 1.041 m/s, respectively. (This figure is available in colour online).

plate is set 500 mm above the domain bottom. The remaining test body volume above the plate is subtracted from fluid domain. Three numerical pressure sensors are located on the plate and water entry velocities are assumed constant. For computational economy, the plate is assumed to be fixed in space and fluid actions apply vertically upwards at speeds 0.519, 0.782 and 1.041 m/s. The free surface is initialised at 30 mm below the plate bottom. This ensured that steady velocity and pressure fields are well developed before impact.

The water entries of symmetric wedges with side wall length of 500 mm and deadrise angles 20, 30, 40 and 60° are modelled within the context of a very thin CFD domain. Similarly, as in plate cases, the wedge is assumed to be fixed in space and the constant water entry velocity is set as 3.13 m/s as the overall scale of model is in agreement with KRISO (2014). The numerical reference domain size in x–z plane is 2 m × 2 m, with the original calm water surface located at the middle of the fluid domain. The wedge apex is positioned in way of the plane of symmetry, i.e. the vertical middle line of the domain (see Figure 2(b)). The sides of the fluid domain that are parallel to the y–z plane are set as symmetry boundary conditions. The wedge surfaces are assumed to be 'walls' representing impenetrable and traction-free surfaces because of inviscid flow assumptions. The domain bottom is set as velocity inlet and the domain top is set as pressure outlet. To suitably idealise fluid dynamics in 2D, the sides of the fluid domain that are parallel to the x–z plane are set as symmetric boundary conditions. Accordingly, the influence of velocity and gradients of all variables normal to the boundary surface is assumed negligible. For the plate case (see Figure 2(a)), the boundary conditions are similar to those applied for the case of the wedge.

The flow is assumed inviscid. Thus, Navier-Stokes equations are reduced to Euler format, as expressed by Equations (1) and (2), respectively (STAR CCM+ 2018):

$$\frac{\partial}{\partial t}\int_V \rho dV + \oint_A \rho \boldsymbol{v} \cdot d\boldsymbol{a} = 0 \tag{1}$$

$$\frac{\partial}{\partial t}\int_V \rho \boldsymbol{v} dV + \oint_A \rho \boldsymbol{v} \otimes \boldsymbol{v} \cdot d\boldsymbol{a} = -\oint_A p\boldsymbol{I} \cdot d\boldsymbol{a} + \int_V \boldsymbol{f}_b dV \tag{2}$$

where ρ is the density, $\boldsymbol{v}$ is the continuum velocity, $\otimes$ is the outer product, $\boldsymbol{f}_b$ is the resultant of the body forces (e.g. gravity) per unit volume acting on the continuum and p is the pressure.

Since FVM approximation is used for both plate and wedge structures, the integral form of conservation equations with initial and boundary conditions is applied to the control volumes and discretised into a set of linear algebraic equations (STAR CCM+ 2018). The second-order upwind scheme is used to evaluate the convective fluxes. The Hybrid Gauss-LSQ method is used to evaluate gradients and the second-order implicit temporal discretisation scheme is used for time integration (STAR CCM+ 2018).

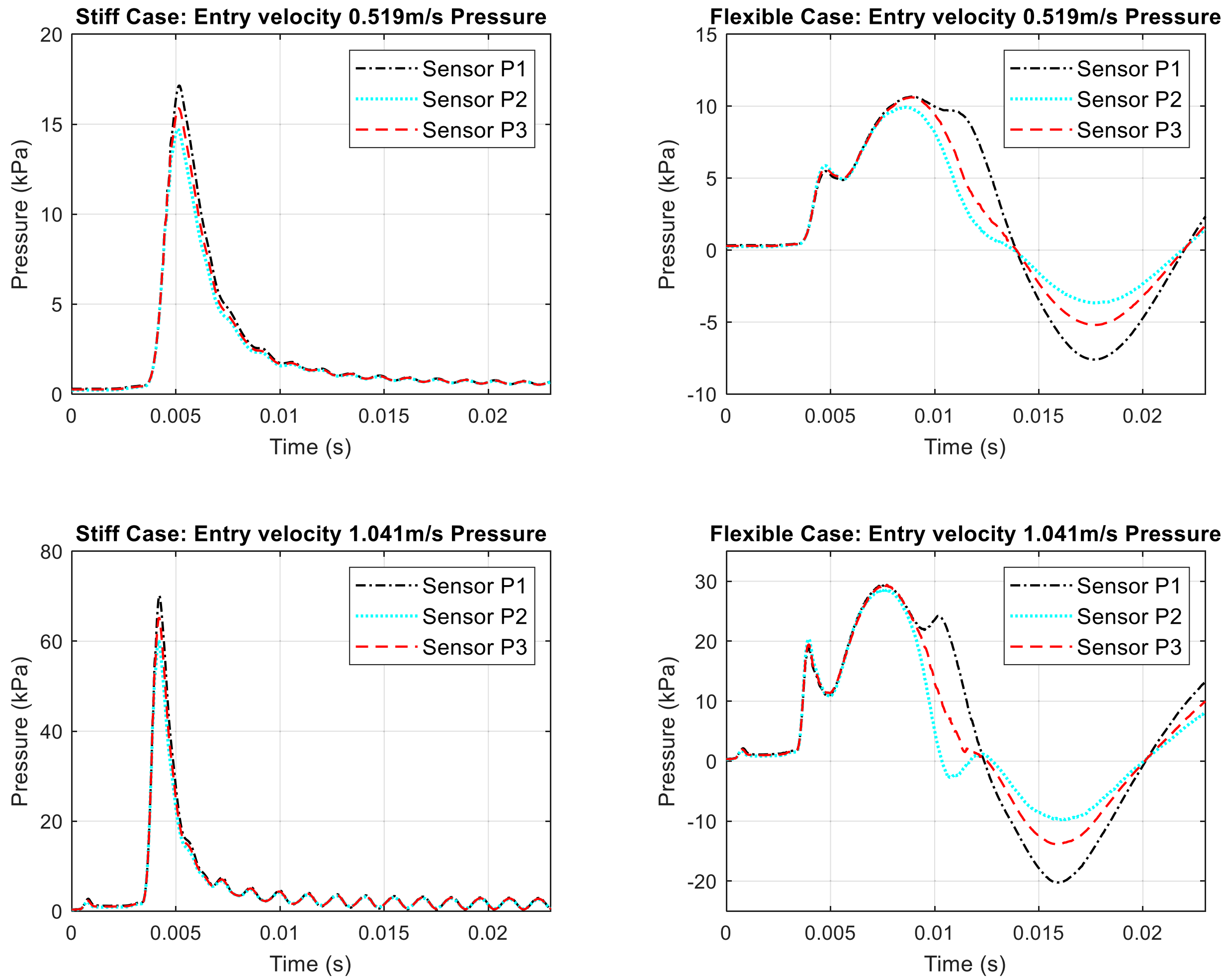

Figure 6. Comparison of stiff and flexible plate simulations results for cases with entry velocity 0.519 and 1.041 m/s, respectively. (This figure is available in colour online).

Eulerian two-phase flow is applied in fluid domain to model both air and water phases. Water compressibility is modelled artificially to enhance numerical stability. Accordingly, density dependency of pressure and speed of sound is idealised as per Lakshmynarayanana (2017) and Camilleri (2017), see Equations (3) and (4). The density of air is assumed constant, considering the ratio of the maximum flow velocity in simulations to the speed of sound in air, i.e. Mach number is much smaller than 0.3.

$$\rho = \rho_0 + p/c^2 \tag{3}$$

$$d\rho/dp = 1/c^2 \tag{4}$$

In the above equations, ρ is the density, ρ_0 is a density constant, $d\rho/dp$ is a derivative of density against pressure and c is the speed of sound in water.

The interface between the phases is modelled by a VOF surface capturing technique (Hirt and Nichols 1981) for which the additional transport equation is solved for a volume fraction. The HRIC (High Resolution Interface Capturing) discretisation scheme is used to discretise the convective fluxes in the volume fraction equation to achieve a sharp resolution of the interface and avoid unphysical solutions.

Unstructured hexahedral cells based on trimmed Cartesian grids are used to discretise both plate and wedge cases (Figure 3). Mesh refinements were carried out by volumetric blocks. This ensured better capturing of the free surface and high gradients of pressure and fluid velocities around the plate and wedge. Southall et al. (2014) generated numerical models of wedges for CFD simulations and compared with the results presented in KRISO (2014). In this work, 5 mm mesh size was applied around the wedge, and comparisons against experimental data were shown to be reasonable while computational cost was modest. On this basis, 5 mm mesh and a time domain discretisation step of the order of 5e–5s may be considered adequate. Based on the work by Yan et al. (2022), 3 mm of grid size was considered adequate in terms of capturing pressure peaks on the plate surface. Time steps of the order of 5e–5s, 4e–5s and 3e–5s are used to idealise small to high-impact water entry.

2.2. Structural domain modelling

The material properties for stiff plate/wedge and flexible plate/wedge are summarised in Table 1. The dynamic response of the wedge and plate structures (i.e. deformations, stresses, strains, etc.) is evaluated using ABAQUS FEA (Dassault Systèmes 2016). In line with the 'hydroelasticity analysis for ship design' approach introduced by Harding et al. (2006), system eigenvalues are evaluated by solving Newton's second law of motion:

$$M\ddot{x} + C\dot{x} + Kx = F \tag{5}$$

where M, C and K are the mass, damping and stiffness matrices, F is the external load applied, $\ddot{x}$, $\dot{x}$, x are the acceleration, velocity and displacement vectors on finite element nodes.

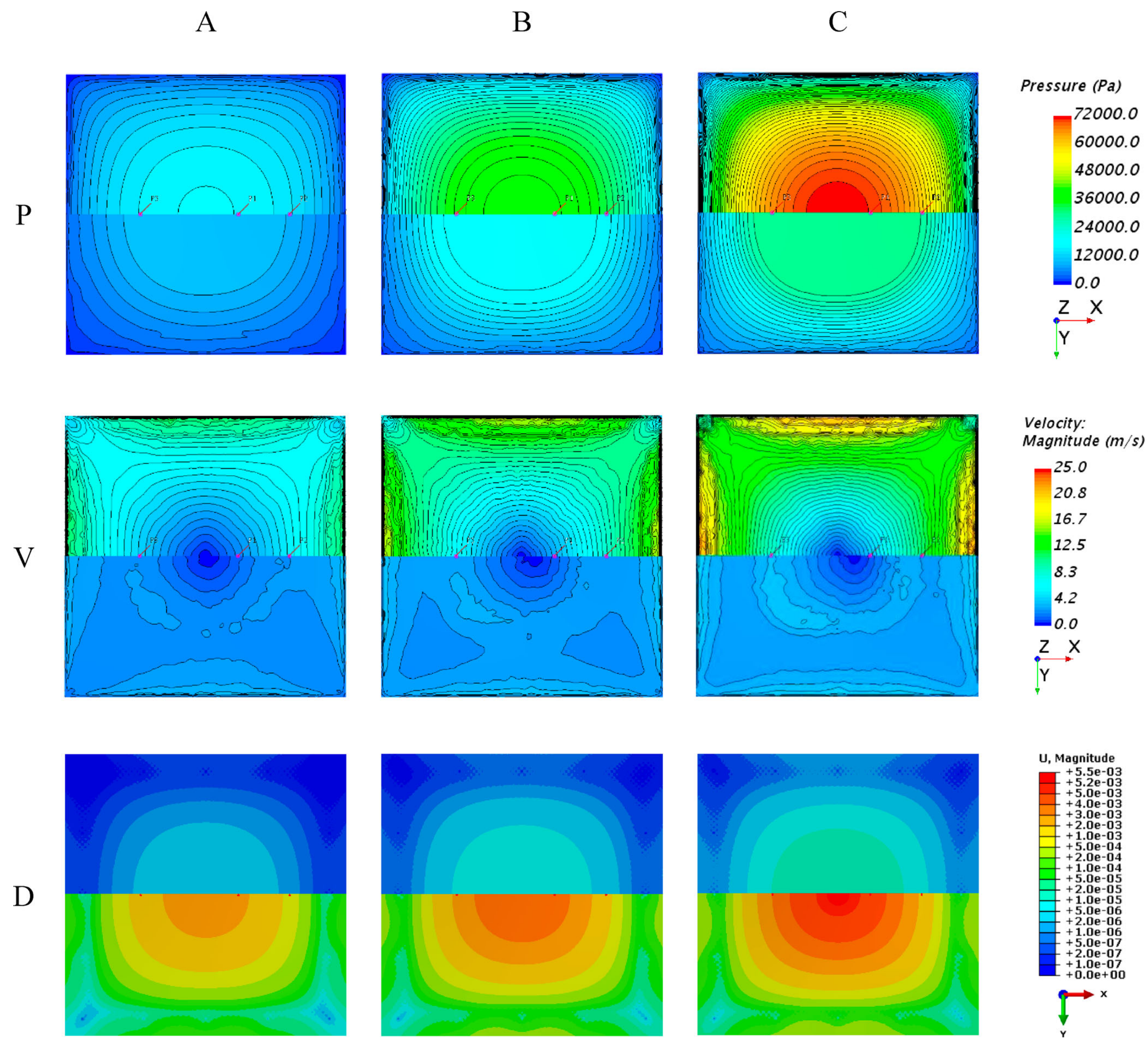

Figure 7. Pressure (P), velocity (V) and deformation (D) distribution at the pressure sensor P1 peak time of impact of stiff plate (upper half) and flexible plate (bottom half) simulations for cases with entry velocity of (A) 0.519 m/s; (B) 0.782 m/s and (C) 1.041 m/s, respectively. (This figure is available in colour online).

The dynamic equilibrium equation is solved by a Lanczos modal analysis algorithm (Dassault Systèmes 2016). When applying the history of loading of slamming pressures, the nonlinear transient dynamic response is calculated using a Hilber–Hughes–Taylor solver for time integration (Bathe 2016). Nonlinear equilibrium equations are solved in an iterative manner at each time increment using Newton's method.

The ABAQUS FEA eight-node continuum shell element (SC8R) is used to discretise the plate/wedge structure. It is noted that this model accounts for the influence of the effects of transverse shear deformation (Dassault Systèmes 2016). Based on the work of Camilleri (2017) and Xiao and Batra (2014), a stiffness proportional Rayleigh damping of the order of 4% is used to diminish the high-frequency components and improve the stability of the numerical solution. Five element stacks are used to idealise the thickness of the plate and to provide better-refined through-thickness response prediction. To ensure better interpolation mapping throughout the two-way coupling process, the discretisation size of structural elements on the plate and wedge bottom surfaces are set similar to those used by the fluid domain model.

The following boundary conditions are applied:

- For the plate structure (see Figure 4(a)), all degrees of freedom (dof) are constraint in way of the 16 vertical screw locations. The translations of outer plate edges are restricted in the *x*- and *y*- directions. The line locations (inner boundary) are constraint along *x*-, *y*- and *z*-translations at 25.3 mm from outer edge of the plate.
- For the wedge structure (see Figure 4(b)), *y*-symmetric boundary condition is applied on the surfaces that are parallel to the *x*–*z* plane. At the top-surface of the wedge structure, *x*-, *y*- and *z*-translations are restricted.

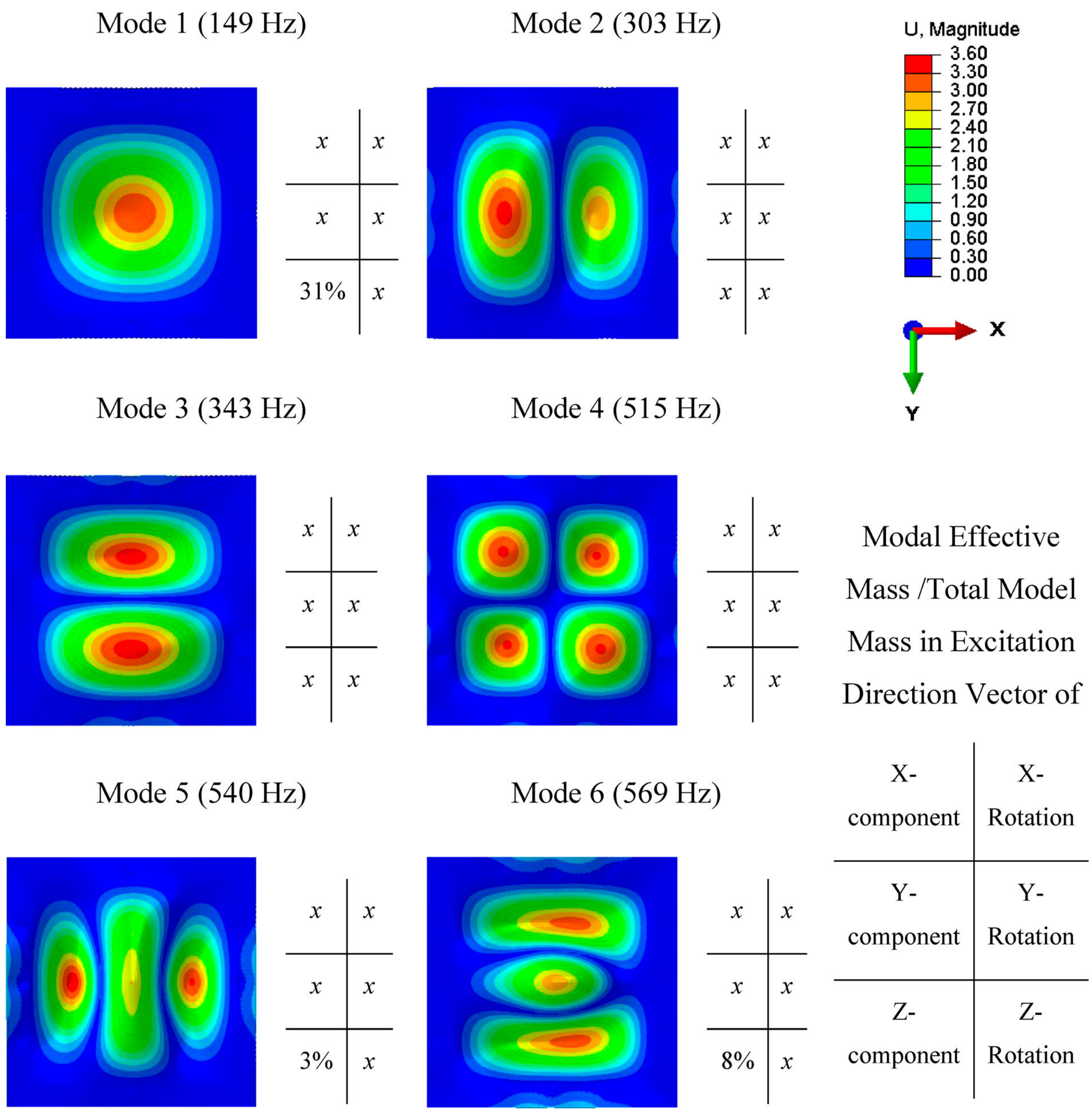

Figure 8. Flexible vibration modes and dry frequencies of POM plate (mode 1–6) (Deformation scale factor 0.01), and corresponding ratio of modal effective mass to total model mass in excitation direction vectors ('x' represents where the ratio is significantly less than 1%). (This figure is available in colour online).

2.3. Two-way fluid–structure interaction (FSI)

A two-way coupled implicit FSI scheme is used to simulate the response of stiff and flexible plates and wedge structures following a slamming event. In two-way coupling, the impact pressure is mapped to the structure, and the structural deformation is transferred back to the fluid solver to update the mesh (Figure 1). An implicit scheme is chosen to idealise the strong coupling between hydrodynamic loads and structural velocities during slamming. In strong coupling algorithms, the fluid and structure solvers can be resident in processor memory simultaneously. Data are then transferred at regular intervals from the memory that the structure solver uses to/from the memory of the fluid solver (STAR-CCM+ 2018). The implicit scheme is computationally expensive. However, it is much more stable as it allows data exchange more than once per time step (20 exchanges per time step is set here, i.e. one exchange per every iteration). The addition of artificial fluid compressibility can benefit the numerical stability and faster convergence of the coupling procedure (STAR-CCM+ 2018).

A partitioned approach during which the fluid and structural simulations rely on independent solvers working in parallel is employed. FSI information exchange is facilitated at each time step of this simulation as Star CCM+ exports hydro-pressures to ABAQUS and imports nodal displacements. When face-centric source data (fluid pressures) are mapped from fluid cells to structural cells, least squares interpolation is used. On the other hand, when node-centric source data (nodal displacements) are transferred from the FE model to FV cells, shape function interpolation is utilised (STAR CCM+ 2018; Lakshmynarayanana 2017).

Mesh morphing is applied to move the fluid vertices to conform to the solid. The 'morpher' firstly uses the control point displacements originated from mesh vertices on the boundary interpolation field. Then, mesh vertices are translated to their new positions. The

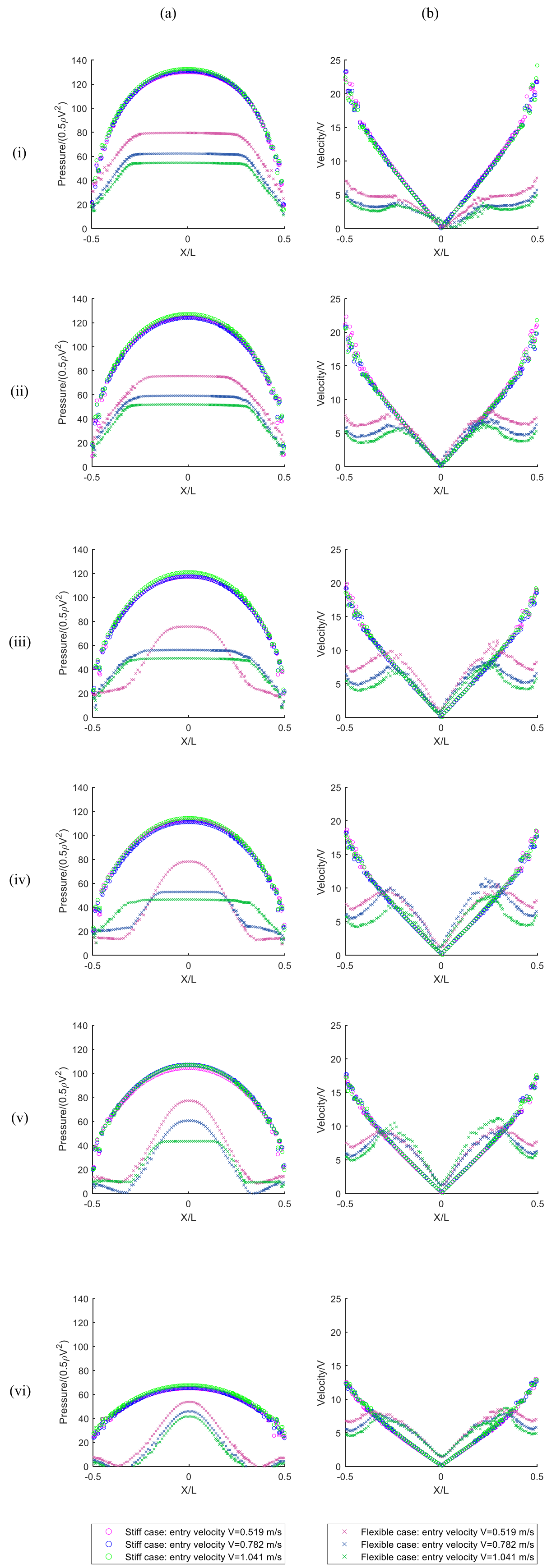

Figure 9. Nondimensional (a) pressure and (b) velocity distributions along the plate centre line ($y = 0$). Both stiff and flexible plates impinging water at velocities 0.519, 0.782, and 1.041 m/s are considered. Results correspond to a time instance for which P1 reaches (i) 100% pressure peak and then sequentially drops to (ii) 95%, (iii) 90%, (iv) 85%, (v) 80% and (vi) 50% of the pressure peak. (This figure is available in colour online).

morphing boundaries (marked as blue text in Figure 2) used in the fluid domain are defined as:

- 'Displacements' for plate/wedge bottom surfaces where mesh vertices move are based on the imported displacement field.
- 'Constraints' where mesh vertices move on the symmetry plane with zero normal displacement.
- 'Fixed points' for all inlets, outlets and other wall surfaces where mesh vertices have zero displacement.

Two-way coupling simulations were run in parallel mode using 40 cores each running at 2.1 GHz of the Intel Xeon 6230 processors of CSC Finland super-computing facility. It took between 20 and 100 h to run 0.1 s of real-time simulation.

3. Results and discussion

3.1. Comparison of impact results on stiff and flexible plates

To validate the FSI model with flexible material properties, plate simulations for three different entry velocities with POM properties are compared against experiments. Figure 5 presents the comparison for pressure sensor P1. Some small fluctuations are not fully captured, and the simulated peaks are a bit lower than the experimental results. It is also shown that the modelling approach is reliable as the pressure histories depicted by comparing simulations against experiments generally match well both in terms of magnitude and frequency.

Comparisons between stiff and flexible plate results show that the pressure of the stiff plate starts to increase to a peak magnitude at the same time as in the flexible case. However, the peak is 'sharper', i.e. the magnitude of the peak is higher than in flexible case while the band is much narrower and stiff plate peaks occur in advance of flexible plate peaks. These results indicate that stiff impacts that are short in duration, happen earlier in time and have higher magnitude. When flexible body dynamics are not considered, there are no large vibration cycles and some small vibrations become evident after the first peak. As the magnitude of the velocity of entry increases, the response of both stiff and flexible peaks amplifies and reduces in bandwidth. Also, the difference of peak pressures between stiff and flexible plates becomes larger.

Pressure histories at different sensor locations for both stiff and flexible cases at the low water entry velocity of 0.519 m/s and higher entry velocity of 1.041 m/s are depicted in Figure 6. For the stiff cases, the general trends do not seem to be affected by the entry velocity, although some differences between peak values become evident. The more central the locations are, the higher the peak and the higher the water entry velocity, the larger the differences between locations. For the flexible cases, the general trend before the pressure peak for the three locations is the same. The central location has the highest peak value. For higher water entry velocity, the pressure peak values also increase, and nearly no differences among their first peaks are observed. This indicates that for higher entry velocities pressures tend to be homogeneously distributed near the central area of the plate.

Figure 7 that presents the spatial distribution of pressure, velocity and deformation components on the bottom of the plate confirms the above. The top and bottom halves of the plate demonstrated on each sub-figure (A, B, C) represent results from stiff and flexible plate modelling, respectively. Stiff plate simulations demonstrate higher magnitudes and wider pressure range. They also demonstrate high velocities and velocity gradients in way of the plate edge. An obvious asymmetric distribution of velocity near

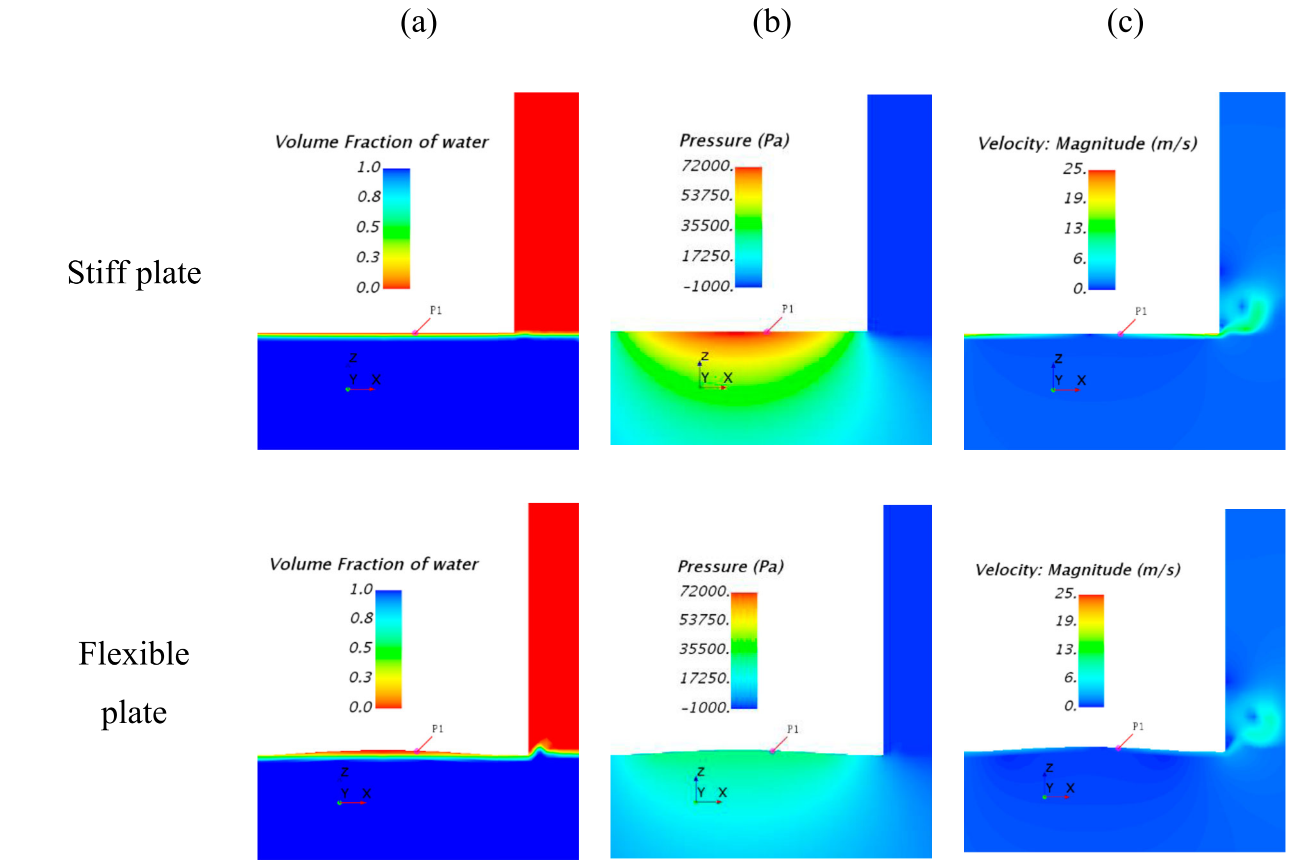

Figure 10. Contours of (a) free surface, (b) pressure and (c) velocity with water entry speed of 1.041 m/s at the peak time (P1). (This figure is available in colour online).

the plate centre becomes evident as the water entry velocity increases with flexible plate simulations. The velocity distribution is symmetric for stiff plate cases. This indicates that higher vibration modes may significantly influence hydroelastic responses. The deformation of a flexible plate is higher than that of a stiff structure. Deformation magnitudes increase with increasing water entry velocity.

Figure 8 demonstrates the natural frequencies and mode shapes of the first six modes for the case of the constrained POM plate, and the corresponding ratio of modal effective mass to total model mass in excitation direction vectors for each mode. The ratio which is significantly less than 1% is represented by 'x'. The purpose of this study has been to further understand the influence of dry modal characteristics on the response. The eigenvectors were normalised so that the generalised mass for each vector is of unit value (Ewins 1984). It appears that plate deflection in the vertical plane dominates the response. This is reflected in the z-component modal effective mass that accounts for 42% of total mass across the first six flexible modes. Whereas mode 1 dominates the response, modes 5 and 6 also contribute. The total effective mass across the first six flexible modes does not reach 50% of the total modal mass value. It may be therefore concluded that higher flexible modes also contain energy levels contributing to the dynamic response. Thus, they cannot be ignored.

The distribution of nondimensional pressures and velocities along the plate centre line ($y = 0$) for the cases of stiff and flexible plates are shown in Figure 9. The figure displays different time instances for which the pressure sensor P1 reaches its peak during water entry and instances for which pressure at P1 sequentially drops to 95%, 90%, 85%, 80% and 50% of its peak pressure. Comparisons of the nondimensional pressure and velocity distributions of stiff plate dynamics do not show clear differences among results corresponding to different water entry velocities. This could be attributed to the relatively low to medium impact velocity range and the air cushioning effect that is not obvious enough for the case of the stiff plate. It is noted that the shapes of distributions keep almost the same amongst different time instances. Their magnitudes decrease with time.

For the flexible plate cases, near the plate centre areas, nondimensional pressure magnitudes decrease while the water entry velocity rises. The magnitudes of the nondimensional pressures are significantly smaller in comparison to those observed for the stiff plate. This indicates that when the entry velocity is higher, a smaller proportion of the kinetic energy is transferred to impact pressure and consequently more energy is absorbed by the plate structure itself during deformation. Exploration of the variational shapes of pressure distributions at different time instances is a worthwhile exercise with flexible cases. At the time instance when the pressure captures by P1 peaks, the pressure distribution shapes become similar amongst different entry velocities. Flexible plate dynamics depict an evenly distributed pressure that is nearly half of that the plate. As shown in Figure 9(iii) over time, the shapes of pressure distributions corresponding to the lowest entry velocity cases change. This change is also obvious in Figure 9(iv) for the mid-entry velocity case and Figure 9(v) for highest-entry velocity case. In Figure 9(vi) (alike Figure 9(i)), similar shapes of pressure distributions are observed again amongst different entry velocities. Regarding the velocity distributions of flexible cases, asymmetric features are demonstrated like shown in Figure 7.

Figure 10 depicts the comparisons of free surface, pressure and velocity magnitudes at a time when P1 reaches its peak for stiff and flexible plate idealisations. Plate deformations are captured well for

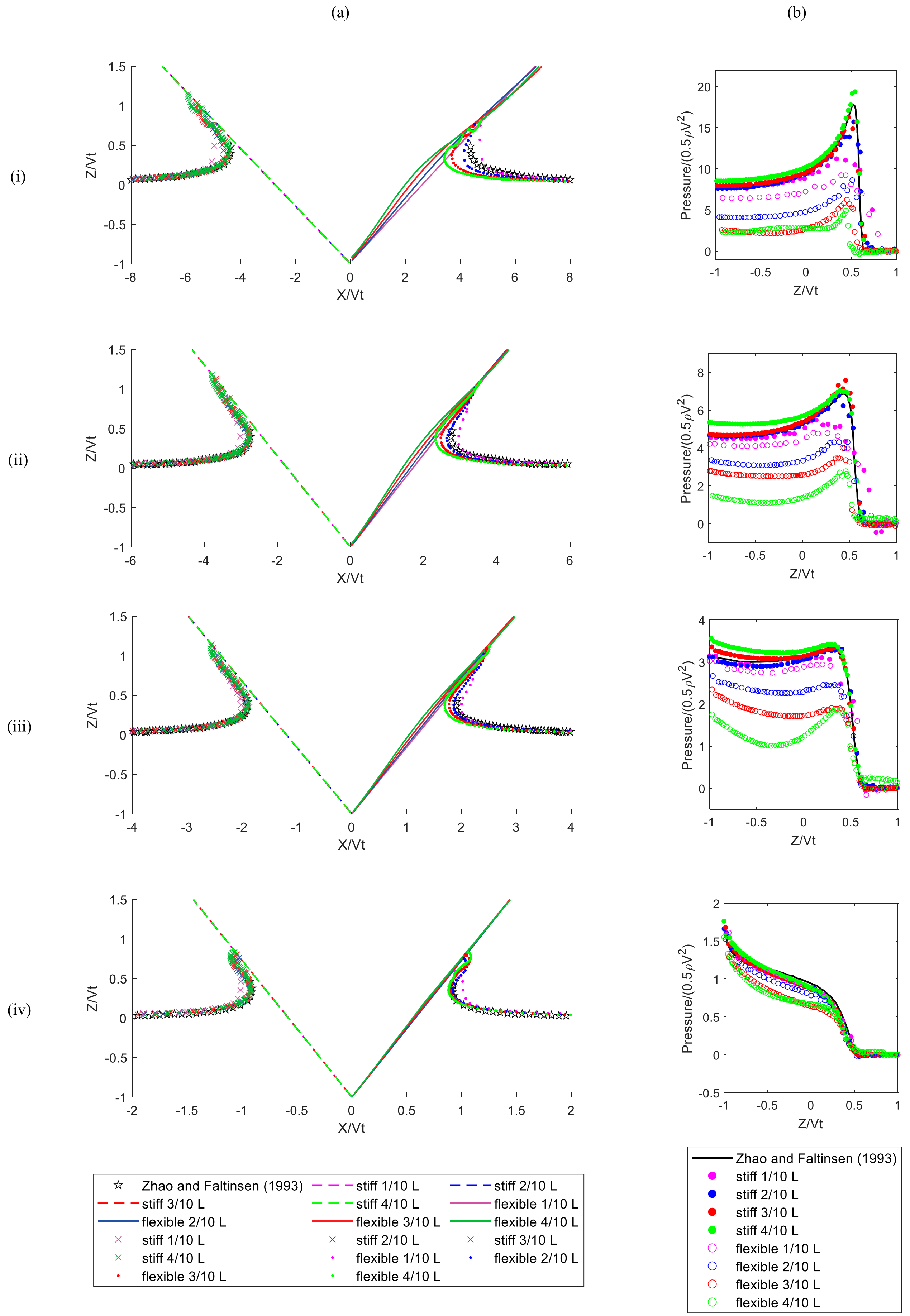

Figure 11. Wedge deformation shape and free surface elevation distributions (a), pressure distribution (b) at the time when water level reaches 1/10, 2/10, 3/10 and 4/10 of wedge side wall length (L) from apex, for (i) 20, (ii) 30, (iii) 40 and (iv) 60° deadrise angle of stiff and flexible wedges. The left halves of (a) represent stiff wedge cases, the right halves of (a) represent flexible wedge cases. (This figure is available in colour online).

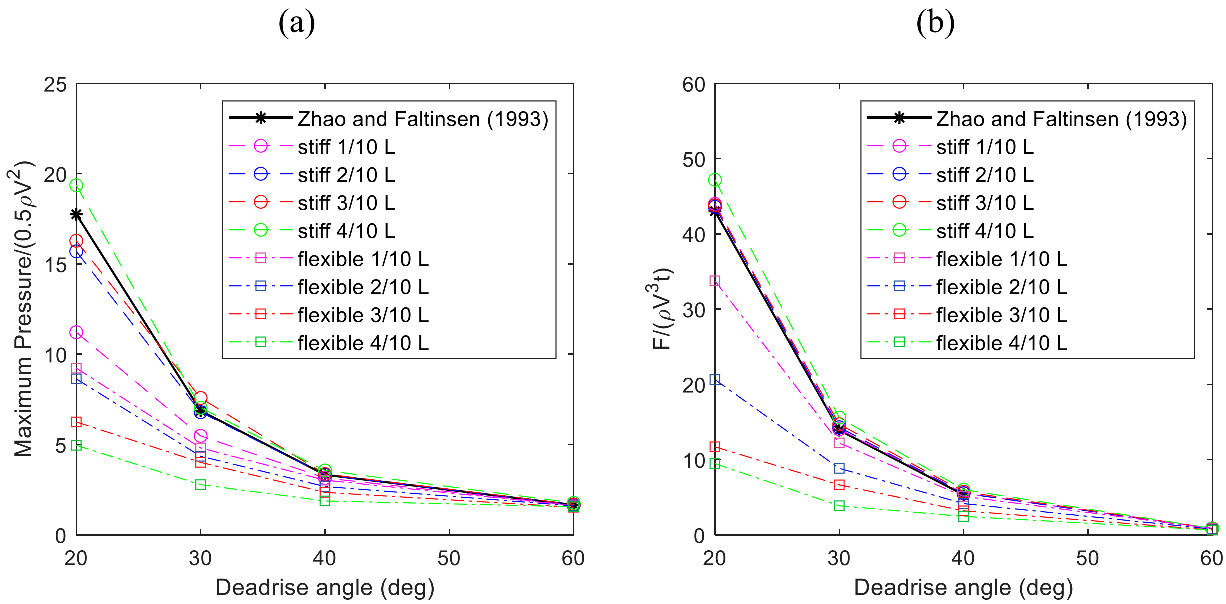

Figure 12. Variations of the (a) nondimensional maximum pressure and (b) total vertical hydrodynamic force on wedge at different wedge deadrise angles (i.e. 20, 30, 40, 60°) for time instances when water level reaches 1/10, 2/10, 3/10 and 4/10 of the wedge side wall length (*L*) from apex. (This figure is available in colour online).

the flexible case, where air is trapped under the deformed flexible plate. Both gradient of pressure and pressure magnitude for the case of the stiff plate are larger than that of the flexible plate case. When comparing velocity magnitude contours, the fluid near the edge of the plate escapes at higher speeds for both stiff and flexible cases. However, the highest velocity magnitude is captured for the stiff case (see Figure 10(c) and Figure 7(VC)).

3.2. Comparison of impact results on stiff and flexible wedge

Numerical simulations of wedge water entries at four different deadrise angles (20, 30, 40 and 60°) were carried out by using the two-way coupled FVM-based CFD and FEA method. Both stiff and flexible material conditions were accounted for. Figure 11 shows the results from both stiff and flexible wedge cases, including wedge deformation shape, free surface elevation and pressure distribution. The results are compared against Zhao and Faltinsen (1993) implemented in classification rules (DNVGL 2017). All values are non-dimensionalised and correspond to time instances when water level reaches 1/10, 2/10, 3/10 and 4/10 of wedge side wall length (*L*) in relation to the apex. To ensure meaningful comparisons against Zhao and Faltinsen (1993), the effect of gravity is not accounted for.

When the stiff wedge dynamics prevail both free surface elevations and pressure distributions match well against Zhao and Faltinsen (1993). When the water level reaches 1/10 of the wedge's side wall length (*L*) from the apex, both free surface elevation and pressure distribution have less similarity in comparison to other time instances. This difference could be attributed to the fact that at the early stages of the impact, the fluid flow and jet are still developing (see Figure 11). The oscillations that are observed near the pressure peak may be related to the pseudo-compressibility of the fluid and instabilities of the numerical schemes applied (e.g. HRIC discretisation scheme). Notwithstanding this, the general trend of pressure distribution remains similar to the one observed by Zhao and Faltinsen (1993) across simulations. For flexible wedge structures, the influence of deformation becomes increasingly obvious at smaller deadrise angles and as the depth of wedge impingement in water increases (Figure 11(a)). Throughout this process, energy transfer leads to different pressure distributions. As shown in Figure 11(b), when the water level reaches 1/10 L, pressure distribution stays relatively close to that obtained for the case of stiff wedge. However, when the water level reaches 2/10 L or 3/10 L, the pressure distribution moves at lower region and when the water level reaches 4/10 L, the pressure distribution pattern changes because of the influence of hydroelastic actions (e.g. see 40° deadrise angle). As water impact develops, the pressure reduces. For example, at 20° deadrise angle, the peak pressure of the flexible wedge reduces to nearly 1/3 in relation to the one observed for the stiff case idealisation. The smaller the deadrise angle, the larger the pressure differences among different time instances.

Figure 12 summarises the nondimensional maximum pressure and total vertical hydrodynamic force of all stiff and flexible cases at different wedge deadrise angles and time instances presented in Figure 11. Results are plotted as a function of different deadrise angles. As the deadrise angle increases, peak pressure and total vertical hydrodynamic force reduce. This observation is equally applicable for both stiff and flexible cases. However, the reductions are more significant with stiff cases. Differences between the simulation results for stiff and flexible wedges are also significant, especially at smaller deadrise angles. The differences between forces among different time instances for flexible wedges are larger. On the other hand, maximum pressure differences among different time instances appear to be modest. The small differences of peak pressure and total hydrodynamic force between the predictions of the stiff model presented in this paper and Zhao and Faltinsen (1993) are expected and may be attributed to the two-way coupled FSI modelling approach. The total vertical hydrodynamic forces of stiff cases are less diverse than maximum pressures as compared to Zhao and Faltinsen (1993), and most likely the averaged values from different time instances will fit better to the line.

Figure 13 presents the nondimensional maximum displacements at different wedge deadrise angles (i.e. 20, 30, 40, 60°) that correspond to different moments in time. The deformations for stiff wedge cases are very small as observed in Figure 11. The displacements of flexible wedges are roughly 100 times larger in magnitude in comparison to those evaluated for stiff cases. The

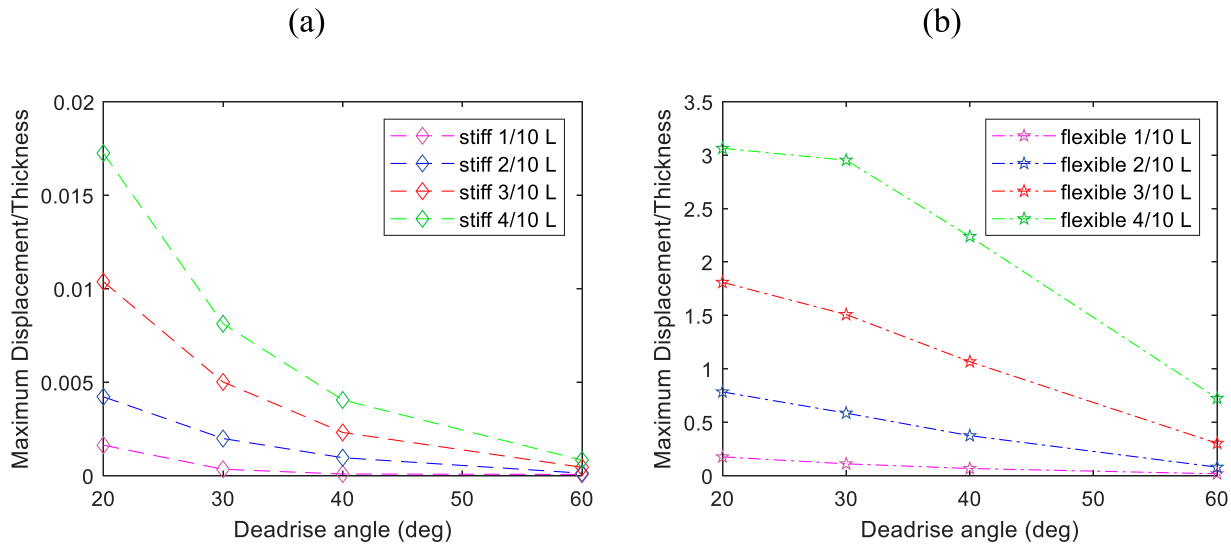

Figure 13. Variations of the nondimensional maximum displacement of (a) stiff wedge and (b) flexible wedge at different wedge deadrise angles (i.e. 20, 30, 40, 60°) for time instances when water level reaching 1/10, 2/10, 3/10 and 4/10 of wedge side wall length (*L*) from apex. (This figure is available in colour online).

displacement of flexible wedge decreases in an almost linear fashion with the increasing deadrise angle. On the other hand, a clearly nonlinear trend is seen for stiff wedge cases.

4. Conclusions

This paper applied a two-way coupled FVM-based CFD-FEA modelling procedure to study the slamming impact on stiff and flexible flat plates and wedge structures. Water entry fluid actions were studied for the cases of a flat plate impinging the water at different velocities and the case of a symmetric wedge idealising slamming at different deadrise angles. Numerical predictions have been compared against available experimental data for flat plates and the hydrodynamic pressure design curves introduced by Zhao and Faltinsen (1993) that are implemented in classification guidelines for wedge-like structures (DNVGL 2017). The results generally showed good agreement. This justifies that the FSI simulation is reasonable. Further comparisons between stiff and flexible FSI dynamics lead to the following conclusions:

- Fluid pressures experienced by stiff and flexible plates increase nearly simultaneously. However, the peak pressure of the stiff plate reaches its maximum earlier, it is higher and lasts less time in comparison to that of the flexible plate.
- Flexible plate FSI demonstrates a negative correlation between the nondimensional pressure and water entry velocity near plate centre area. In addition, air entrapment is evident. However, this is not the case for stiff plates, where the same topology is considered at those relatively low to medium impact velocities.
- A two-way coupled FVM-based CFD-FEA modelling procedure does not change the trend of pressure design curves already implemented in classification rules for stiff wedges.
- The smaller the deadrise angles, the larger the differences of fluid pressures and forces between stiff and flexible structures. Similarity in the pressure distributions of flexible wedges is not obvious.

Overall, the modelling of slamming impacts demonstrates that accounting for the structural flexibility is important in terms of predicting pressure peak magnitudes for wedge-type structures. This is because structural flexibility can inherently damp out high amplitude and transient slamming impulses. Future research will focus on understanding the influence of flexibility on different levels of dynamic response (dynamic amplification factors) with the ultimate aim to select the most appropriate method for use in ship design.

Acknowledgements

The authors wish to acknowledge CSC – IT Center for Science, Finland, for the provision and use of their computational resources. The authors also wish to acknowledge experimental data available in Tödter et al. (2020).

Disclosure statement

No potential conflict of interest was reported by the author(s).

Funding

This work was supported by Aalto University.

ORCID

Dongni Yan http://orcid.org/0000-0003-4450-3462
Tommi Mikkola http://orcid.org/0000-0001-6109-3536
Pentti Kujala http://orcid.org/0000-0003-2665-9957
Spyros Hirdaris http://orcid.org/0000-0002-4700-6325

References

Alexandru I, Brizzolara S, Viviani M, Couty N, Donner R, Hermundstad O, Kukkanen T, Malenica S, Termarel P. 2007. Comparison of experimental and numerical impact loads on ship-like sections. In: Guedes SC, Das PK, editors. *Advancements in marine structures*. London: Taylor and Francis; p. 339–349.

ASME. 2009. Standard for verification and validation in computational fluid dynamics and heat transfer: ASME V&V 20. American Society of Mechanical Engineers.

Bathe KJ. 2016. Finite element procedures. Prentice Hall: Pearson Education. ISBN 978-0-9790049-5-7.

Camilleri J. 2017. Experimental and numerical investigation of slamming loads on high-speed craft including hydroelastic effects [Doctoral Thesis]. Southampton, UK: University of Southampton.

Dassault Systèmes. 2016. Abaqus theory guide. Providence, RI.

DNVGL. 2017. Environmental conditions and environmental loads. Det Norske Veritas. Recommended Practice. DNVGL-RP-C205.

Ewins DJ. 1984. Modal testing: theory and practice. Letchworth: Research Studies Press.

Farsi M, Ghadimi P. 2016. Effect of flat deck on catamaran water entry through smoothed particle hydrodynamics. *Proc Inst Mech Eng M J Eng Mar Environ*. 230(2):267–280.

Ferziger J, Peric M. 2003. Computational methods for fluid dynamics. 3rd ed. Berlin: Springer.

Harding RD, Hirdaris SE, Miao SH, Pittilo M, Temarel P. 2006. Use of hydroelasticity analysis in design. Proceedings of the 4th International Conference on Hydroelasticity in Marine Technology; Sep 10–14, 2006. Beijing, China: National Defense Industry Press. p. 1–12. ISBN: 7-118-04728-7.

Hirdaris SE, Bai W, Dessi D, Ergin A, Gu X, Hermundstad OA, Huijsmans R, Iijima K, Nielsen UD, Parunov J, et al. 2014. Loads for use in the design of ships and offshore structures. Ocean Eng. 78:131–174.

Hirdaris SE, Temarel P. 2009. Hydroelasticity of ships: recent advances and future trends. P I Mech Eng M: *J Eng Maritime Environ*. 223(3):305–330.

Hirt C, Nichols B. 1981. Volume of fluid method for the dynamics of free boundaries. J Comput Phys. 39, 201–225.

Joint Accident Investigation Commission (JAIC). 1997. Final report on the capsizing on 28 September 1994 in the Baltic Sea of the Ro-ro passenger vessel MV Estonia. Helsinki: Edita Books.

Kapsenberg GK. 2011. Slamming of ships: where are we now? Philos Trans Royal Soc A. 369(1947):2892–2919.

Kivelä E, Lakshmynarayanana PA, Hirdaris S. 2020. Coupled CFD and FEA to predict the dynamic structural response of modern cruise ship deck outfitting due to wind-induced vibrations. Proceedings of the ASME 2020 39th International Conference on Ocean, Offshore and Arctic Engineering. Volume 2A: Structures, Safety, and Reliability. Virtual, online; Aug 3–7, 2020. V02AT02A029. ASME.

KRISO. 2014. Wave induced loads on ships – joint industry project III – interim report. MOERI Technical Report No. BSPIS7230-10572-6.

Lakshmynarayanana PAK. 2017. Application of 3-D CFD modelling for dynamic behavior of ship in waves [Doctoral Thesis]. Southampton, UK: University of Southampton.

Lakshmynarayanana PAK, Hirdaris S. 2020. Comparison of nonlinear one- and two-way FFSI methods for the prediction of the symmetric response of a containership in waves. Ocean Eng. 203(2020):107179.

Lu CH, He YS, Wu GX. 2000. Coupled analysis of nonlinear interaction between fluid and structure during impact. J Fluid Struct. 14:127–146.

Maki KJ, Lee D, Troesch A, Vlahopoulos N. 2011. Hydroelastic impact of a wedge-shaped body. Ocean Eng. 38:621–629.

Panciroli R, Abrate S, Minak G, Zucchelli A. 2012. Hydroelasticity in water-entry problems: comparison between experimental and SPH results. Compos Struct. 2012(94):532–539.

Southall N, Choi S, Lee Y, Hong C, Hirdaris S, White N. 2015. Impact analysis using CFD – a comparative study. Proceedings of the 25th International Ocean and Polar Engineering Conference; Kona, Hawaii, USA. ISOPE-I-15-0675.

Southall N, Lee Y, Michael C, Hirdaris S, White N. 2014. Towards a pragmatic method for prediction of whipping: wedge impact simulations using OpenFOAM. Proceedings of the 24th International Ocean and Polar Engineering Conference (ISOPE); Busan, South Korea. ISOPE-I-14-341.

STAR CCM+. 2018. User manual for STAR CCM+. Sabalcore, Florida.

Stenius I, Rosn A, Kuttenkeuler J. 2006. Explicit FE-modeling of fluid-structure interaction in hull-water impacts. Int Shipbuild Prog. 53:1031–1121.

Stenius I, Rosn A, Kuttenkeuler J. 2011. Hydroelastic interaction in panel-water impacts of high-speed craft. Ocean Eng. 38:371–381.

Tödter S, el Moctar O, Neugebauer J, Schellin TE. 2020. Experimentally measured hydroelastic effects on impact-induced loads during flat water entry and related uncertainties. J Offshore Mech Arct Eng. 142:011604-1.

Truong DD, Jang BS, Janson CE, Ringsberg JW, Yamada Y, Takamoto K, Kawamura Y, Ju HB. 2021. Benchmark study on slamming response of flat-stiffened plates considering fluid-structure interaction. Marine Struct. 79:1–28.

Veen DJ, Gourlay TP. 2012. A combined strip theory and smoothed particle hydrodynamics approach for estimating slamming loads on a ship in head-seas. Ocean Eng. 43:64–71.

von Karman T. 1929. The impact on seaplane floats during landing. National Advisory Committee for Aeronautics Technical Notes: 321.

Wagner H. 1932. Über Stoß- Und Gleitvorgänge an Der Oberfläche von Flüssigkeiten. Z Angew Math Mech. 12(4):193–215.

Wang S, Guedes Soares C. 2012. Water impact of symmetric wedges with a multi-material Eulerian formulation. Int J Maritime Eng. 154(A4):191–206.

Wang S, Guedes Soares C. 2014. Numerical study on the water impact of 3D bodies by explicit finite element method. Ocean Eng. 78:73–88.

Xiao J, Batra RC. 2014. Delamination in sandwich panels due to local water slamming loads. J Fluids Struct. 48(2014):122–155.

Yamamato Y, Iida K, Fukasawa T, Murakami T, Arai M, Ando A. 1985. Structural damage analysis of a fast ship due to bow flare slamming. Int Shipbuild Progr. 32:124–136.

Yan D, Mikkola T, Lakshmynarayanana A, Tödter S, Schellin TE, Neugebauer J, el Moctar O, Hirdaris S. 2022. A study into the FSI modelling of flat plate water entry and related uncertainties. Marine Struct. 86, p.103296.

Zhao R, Faltinsen O. 1993. Water entry of Two-dimensional bodies. J Fluid Mech. 246(4):593–612.

Zhao R, Faltinsen O, Aarsnes J. 1996. Water entry of arbitrary two-dimensional sections with and without flow separation. Proceedings of the 21st Symposium on Naval Hydrodynamics. Washington, DC: National Academy Press. p. 408–423.